Zhang, Y., Mo, D., Han, X., Xu, J., Wang, C., Huang, L., & Wu, K. (2023). A high-Q acoustic filter based on programable electromechanical Fano resonance. *Mechanical Systems and Signal Processing*, *191*,
doi:110177. 10.1016/j.ymssp.2023.110177

A high-Q acoustic filter based on programable electromechanical Fano resonance

Yumin Zhang[a], Di Mo[a], Xue Han[b], Jiawen Xu[c], Chunqi Wang[d], Lixi Huang[b]*, Keming Wu[b]*

[a] *Foshan University 33 Guangyun Road, Shishan, Nanhai District, Foshan, Guangdong Province, China*

[b] *Department of Mechanical Engineering, The University of Hong Kong, Pokfulam Road, Hong Kong*

[c]*School of Instrument Science and Technology, Southeast University, Nanjing, China*

[d]*Johnson Electric, Hong Kong Science Park Shatin, NT Hong Kong*

**Corresponding author, E-mail: kemingwoo@foxmail.com, lixi@hku.hk*

Phone: 852-39172627; Fax:852-28585415

Abstract

Fano resonance with a sharp and ultra-narrow asymmetrical spectral profile is formed by interfering a background mode by a local mode, which is widely found in numerous physical areas and serves as a bedrock for architecting functional metamaterials and constructing selective filters for physical waves. However, it requires subtle geometries and accurate mechanical properties for generating a local resonance to realize Fano resonance at a desired frequency, which challenges its widely applications. Here, we report an electromechanical Fano resonance delivered by an electromechanical diaphragm shunted by a multiple-branch resonant circuit (SEMD). The local resonance of the SEMD is induced by the electrical circuit, which removes the constraints of subtle geometries and mechanical properties design and allows digitally programing the Fano resonance through coding MOSFET switches to select a preset circuit branch. A Lumped theoretical model is used to analyze circuit effects, with verification by experiments in a one-dimensional waveguide, showing programing of three key parameters, the frequency, Q factor and extinction ratio (ER), of the electromechanical Fano resonance. The frequency of perfect sound absorption (null reflection) digitally assigned in a frequency range of [158.5 Hz 1486.75 Hz] is experimentally demonstrated, equivalent to a wavelength-to-thickness ratio range of [31.6 0.30], regarding the equivalent thickness of the SEMD. The Q factor of the SEMD, indexing the selectivity, can be tuned up to 145 in experiments and over 6000 theoretically, giving the half-bandwidth less than 0.2 Hz. The extinction ratio (ER) reaches 30 dB in experiments whereas 60 dB in predictions which means the circuit can totally change the acoustic response of the mechanical diaphragm. Due to features of real-time programmability, broadband tunability and mechanical properties and geometries independence, the SEMD with an electromechanical Fano resonance would be a superior platform to fulfill the envisaged manipulation of acoustics waves in a digital manner.

Key words: Fano resonance; Electromechanical coupling; Programable acoustics device; Selective acoustics filter; High-Q device

1. Introduction

A local resonance interfering with a continuous spectrum forms the Fano resonance [1–3], which is first identified by Ugo Fano in his analysis of Beulter's experimental results of noble gases absorption spectra[4]. Contrasting to the traditional symmetrical resonance profile, such as Lorentz resonance and Breit-Wigner resonance, Fano resonance gives an asymmetrical spectrum shape with an unusual pair of adjacent sharp dip and peak. It occurs widely in micro and macro structures [5–7], and across many fields including quantum mechanics[8–10], optics [11,12], biology and chemistry [13]. In the vicinity of the frequency of Fano resonance, the absorptance, transmittance or reflectance vary between unity and zero drastically, which are referred as "dark state" and "bright state", respectively. This property makes it an indispensable core of metamaterials for various functionalities [5,6,14] including inducing transparency or opacity [15,16] for wave transmission, high-Q filter [17] and slowing light[18] and so on.

Fano resonance is also widely found in acoustics and vibration [19–21]. In the theoretical analysis of bound states in the continuum (BSC) [22,23], also known as embedded trapped modes, it is found that, when the geometrical symmetry is broken, the BSC is identical to a Fano resonance [24], which creates band gaps for sound transmission in a duct [25–27]. It's also adopted for constructing acoustic meta-surface such as assembling an array of Fano-resonant cells to form a flat Fresnel reflector [28]. By combining different geometries to produce Fano resonances and taking benefit of "bright mode" or "dark mode", perfect sound reflection or absorption [29,30] is successfully achieved. Other breakthroughs by acoustic Fano resonance include directional sensing [31], high-Q, dual-band filter [32].

It requires a finest design of geometries to produce Fano resonance at desired frequency to match the target. In addition, practices require manipulating sound waves at different frequencies by different magnitudes and bandwidths while the geometry dependence prevents shaping the spectrum profile of a Fano resonance at will. These conflicts spur the research of tunable Fano resonance in various areas. Conventional methods of tuning the Fano resonance include morphing geometries [33,34] and the redesign of the dimensions of the local resonator or background structures for tuning the Fano resonance [35,36]. Tuning Fano resonance by active external fields and excitations is also feasible and preferable, most of which are realized

in optics and plasmonics. Effective mechanisms include optical pump induced nonlinear effects to alter the coupling of two modes [37], Fermi energy regulated local resonance frequency of graphene metamaterials [38,39], shifting local resonance frequency by voltage-controlled liquid crystals [40,41].

The narrow-band nature of the Fano resonance inspires us to create a high-Q filter for sound wave which is demanded in many applications, such as removing narrow band noise from background radiation, eliminating acoustic modes without interfering a broadband sound field and selective sensing of sound wave, etc. Unfortunately, tuning methods for acoustic Fano resonance still rely on sophisticated modification of geometries and their dimensions, which prevents the forementioned filter from widely applications in sound wave manipulations.

Here, we present a shunted electromechanical diaphragm (SEMD) with a programmable Fano resonance to create a high-Q filter for sound waves in duct. The Fano resonance is induced by interfering the background resonance of a spring-mass system (the suspended diaphragm) with the local resonance of an electrical circuit through electromechanical coupling of a moving-coil immersed in a magnetic field. The local mode is fully governed by electrical parameters instead of geometrical and mechanical parameters. It allows us to program the Fano profile of the SEMD digitally through activating a preset circuit branch by its cascaded MOSFET, which is as a voltage controlled electronic switch. The Fano profile has three key parameters, which are frequency of Fano resonance, Q factor and extinction ratio (ER). Being able to program the frequency of Fano resonance digitally means that the constraints of mechanical and geometrical are removed. Achieving a high Q factor represents realization of a highly selective acoustics filter by the SEMD, and a high ER suggests that the circuit can totally change the acoustic response of the diaphragm. By demonstrating coding of these parameters in an electrical manner, we march a step to our ambition of digital control of physics waves. Meanwhile，temporal programing of electrical circuit is easy and the MOSFET has a rapid response (up to a megahertz), the SEMD would also be a superior platform to investigate the temporal-modulated metamaterials [42–45] .

In following sections, we firstly introduce the lumped parameter model of the SEMD in Section 2, based on which multi-physics mechanisms of the electromechanical Fano resonance

is analyzed and the resultant sound reflection and absorption spectra are investigated. In Section 3, effects of circuit components on the Fano profile are parametrically inspected, from which the strategies of reshaping the frequency, Q factor and extinction ratio of the Fano profile is summarized. Experimental results are presented in Section 4, which verifies theoretical analysis.

2. Electromechanical Fano resonance of the SEMD

A shunt moving-coil is used to realize the SEMD in this work. Shunt techniques based on piezoelectric (PZT) plate [46–49] and dielectric elastomer [50,51] are often used for constructing smart structure for vibration isolation [52]. However, PZT plate is too rigid to respond to low-frequency sound wave, and the apparent density mismatching of PZT material and air invalidates it for controlling sound wave in a broad bandwidth (such as over 2 octaves). The shunt moving-coil, due to its versatile configurability, works effectively both in sound absorption and isolation [53–55], and vibration control [42,43,56,57]. The moving-coil with a diaphragm is with a small dynamics mass and low stiffness with a proper design, which is preferred for manipulating sound wave in air. Therefore, the shunt electromechanical diaphragm is adopted for constructing the electromechanical Fano resonance and further the high-Q acoustics filter in this work.

2.1. Lumped parameter model for SEMD

The schematic of the SEMD with an electromechanical Fano resonance is shown in Fig. 1(a). A suspended diaphragm, which is equivalent to a spring-mass oscillator below its piston frequency (no flexural mode), is attached to a moving-coil subjected to a DC magnetic field with magnetic flux density B. The terminals of the moving-coil connect to a multi-branch shunt circuit, each branch is a resonant R-L-C circuit. As the incident sound pushes the diaphragm, the moving-coil cuts the magnetic field and generates an electromotive force (E) across the coil, which drives the electrical current (I) in the shunt circuit. The charged coil in the DC magnetic field is subjected to a Lorentz force (F_e). This force is equivalent to an electrically induced acoustic (EIA) impedance (ΔZ), which is added to mechanical impedance of the diaphragm and changes the dynamic response of it. The circuit resonance, therefore, interferes with the acoustic

oscillator (the diaphragm).

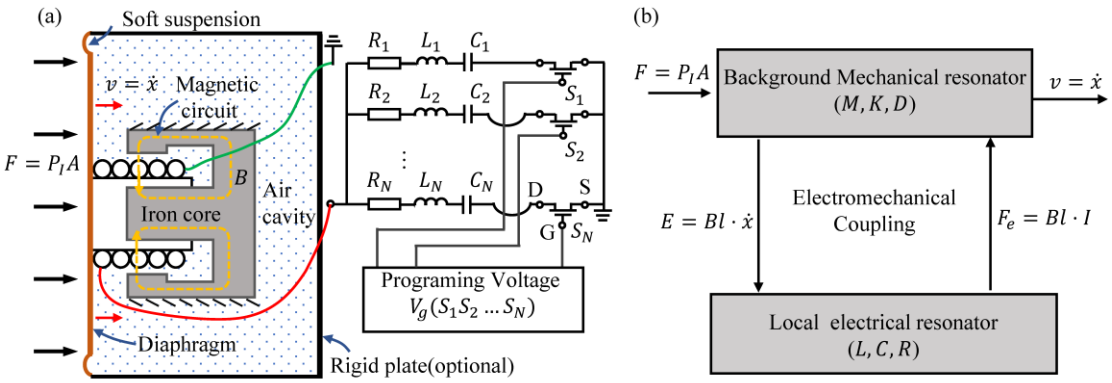

Figure 1: Schematic of the SEMD for programmable Fano resonance. (a) Moving-coil loudspeaker shunted by an R-L-C circuit. The suspended diaphragm is regarded as a spring-mass system whose dynamic mass, stiffness and damping are denoted by M, K and D, respectively. P_I is the complex amplitude of the incident sound wave on the surface of the diaphragm. The moving-coil with effective length of l is subjected to magnetic field with magnetic flux density B, giving a force factor of Bl. (b) Diagram of electrical resonance interfering with the acoustic resonance.

Schematic in Fig. 1 is for theoretical model, The R_N and L_N in the circuit already include the coil resistance and inductance. The full implementation of SEMD is shown in later section, in which the negative impedance converter circuit is introduced. It allows R_N and L_N to approach zero, otherwise the lowest values of R_N and L_N are limited by the coil resistance and inductance.

The coupling diagram is shown in Fig. 1(b). The coupling strength is determined by the product of the magnetic flux density (B) and the effective length of the coil (l). Each branch of the circuit cascades an NPN-type MOSFET, which serves as an electronic switch controlled by the voltage signal supplied to the gate (G) port of it. Its effective electrical resistance between the drain (D) and source (S) ports, R_{ds}, is ideally zero and 4 mΩ in practice when the gating voltage is above a threshold (2V ~4 V normally), and infinity below the threshold. The on-off states of the MOSFETs are noted by S_n, where $S_n = 1$ means the n^{th} branch is switched on, and $S_n = 0$ means the branch is switched off. Ideally, a circuit with N branches produces 2^N states

space for the system. In this study, we limit ourselves to one branch being switched on at any time to elucidate the mechanism of programing the Fano resonance.

The SEMD can work as a termination or and a partition for a sound wave in a 1-dimensional (1D) duct. Fig. 2(a) shows the former case. An incident wave with a complex amplitude of P_I, which is a plane wave below the cut-off frequency of the duct, forces the diaphragm of the SEMD to vibration with a velocity v and consequently produces the reflected wave with complex amplitude of P_R. In this case, the SEMD is a filter for reflected wave, and the overall loading to the incident wave includes the impedance of the SEMD and the fluid loading (air) in the waveguide, while the enclosed air at the termination provides additional stiffness to the suspension of the SEMD. Fig. 2(b) shows SEMD working as a filter for the transmitted wave with complex amplitude of P_T. The fluid loading turns out to be $2Z_0 = 2\rho_0 c_0 A$, which includes fluid loading of upstream and downstream of the waveguide.

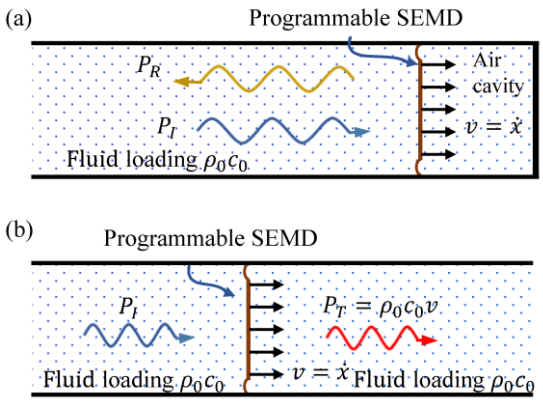

Figure 2: Schematic of SEMD in a one-dimensional waveguide. (a) SEMD at the end of waveguide as a sound absorber. The fluid loading in upstream is $Z_0 = \rho_0 c_0 A$, which is the normalization factor for the acoustic impedance of the SEMD. (b) SEMD partitioning the waveguide for transmitted wave filtering.

With the 1D models shown in Fig. 2(a), a lumped parameter model of the SEMD is derived. With one circuit branch switched on, the dynamics is described by Eq. (1)

$$\begin{bmatrix} Z_m + Z_0 & Bl \\ -Bl & Z_e \end{bmatrix} \begin{bmatrix} i\omega X \\ i\omega Q \end{bmatrix} = \begin{bmatrix} 2P_I \\ 0 \end{bmatrix}, \tag{1}$$

where ω is the angular frequency, A is the effective area of the diaphragm, Bl is the magnetic

force factor, $Z_m = i\omega M + D + K/(i\omega)$ is the mechanical (acoustic) impedance of the diaphragm, $Z_e = i\omega L + R + 1/(i\omega C)$ is the electrical impedance of the shunt circuit, and X is the diaphragm displacement and Q is the electrical charge. Noted that the stiffness K includes the stiffness of the air cavity, namely, $K = K_d + K_0$, where K_d is the suspension stiffness of the diaphragm and K_0 is the stiffness of the air cavity. Using the overall stiffness K we can calculate a equivalent thickness $Th = \rho_0 c_0^2 A/K$ which will be used to deduce the wavelength-to-thickness ratio indicating the deep-subwavelength performance of the SEMD. It should be also noted that the coil resistance and inductance are also included in R and L.

In this work, we focus on the study of the SEMD working as a reflection filter and sound absorber shown in Fig. 2(a). If we change the fluid loading term from Z_0 to $2Z_0$, Eq. (1) and following derivations also work for SEMD acting as an intermedia layer filtering transmitted waves as shown in Fig. 2(b). The vibration velocity of the diaphragm is formulated as

$$i\omega X = \frac{2P_I A}{Z_m + Z_0 + (Bl)^2/Z_e} \tag{2}$$

where

$$Z_s = Z_m + Z_0 + (Bl)^2/Z_e \tag{3}$$

is the mechanical impedance of the system. $\Delta Z = (Bl)^2/Z_e$ is the EIA impedance. Without the coupling, the resonance frequencies of the diaphragm and the circuit are $f_m = \sqrt{K/M}/2\pi$ and $f_e = \sqrt{1/(LC)}/2\pi$, respectively.

As Fig. 2(a) shows, the velocity continuity condition links the incidence, reflectance, and the displacement of the diaphragm, namely, $P_I - P_R = \rho_0 c_0 v = \rho_0 c_0 (i\omega X)$, which gives the sound reflection coefficient of the SEMD as

$$\beta = |P_R/P_I|^2 = \left|1 - \frac{i\omega X Z_0}{P_I A}\right|^2 = \left|\frac{\bar{Z}_m + \Delta\bar{Z} - 1}{\bar{Z}_m + \Delta\bar{Z} + 1}\right|^2, \tag{4}$$

where $\bar{Z}_m = Z_m/Z_0$ is the normalized acoustic impedance and $\Delta\bar{Z} = (Bl)^2/(Z_e Z_0)$ is the normalized EIA impedance. The sound absorption coefficient, therefore, is

$$\alpha = 1 - \beta = \frac{4(\bar{Z}_m + \Delta\bar{Z})_r}{(\bar{Z}_m + \Delta\bar{Z} + 1)_r^2 + (\bar{Z}_m + \Delta\bar{Z})_i^2}, \tag{5}$$

where subscripts "*r*" and "*i*" represent real and imaginary parts of the impedances in the brackets, respectively. Without the coupling, namely, $\Delta\bar{Z} = 0$, Eqs. (4) and (5) describe the sound reflection and absorption coefficients for a simple spring-mass system, from which we

can conclude the well-known impedance matching conditions for perfect sound absorption: $\bar{Z}_m = 1$. It requires the diaphragm to have zero reactance and a damping identical to that of air, which is impossible over a broad frequency band. Zero reactance is only achieved at the resonance frequency by a proper mass addition design. In this work, we couple a programmable electrical resonance to the mechanical resonance to obtain the Fano profile and achieve a versatile spectral shaping for the absorption and reflection without involving any geometrical modification. When the coupling is activated, the EIA impedance $\Delta\bar{Z}$ is engaged, which produces an asymmetrical absorption and reflection spectra shown in Fig. 3.

2.2. Fano resonance of the SEMD

In the following content, we will show that the SEMD, with the coupling of mechanical and electrical resonances, produces a Fano resonance.

Eq. (1) can be rewritten as

$$\begin{bmatrix} -\omega^2 + i\gamma_m\omega + \omega_m^2 & i\omega Bl/M \\ -i\omega Bl/L & -\omega^2 + i\gamma_e\omega + \omega_e^2 \end{bmatrix} \begin{bmatrix} X \\ Q \end{bmatrix} = \begin{bmatrix} P_0 \\ 0 \end{bmatrix}, \tag{6}$$

where $\gamma_m = (D + Z_0)/M, Z_0 = \rho_0 c_0 A$, $\gamma_e = R/L$, $\omega_m = \sqrt{K/M}$, $\omega_e = 1/\sqrt{LC}$, $P_0 = 2P_I/M$, $i = \sqrt{-1}$.

Without the coupling, the two coupling terms in Eq. 6, $i\omega Bl/M$ and $-i\omega Bl/L$, are omitted. The circuit system and diaphragm system are independent and with original resonance frequencies of $\omega_m = 2\pi f_m$ and $\omega_e = 2\pi f_e$, respectively. With the coupling, ω_m shifts to ω_1 and ω_e shift to ω_2. ω_2 is the frequency of the Fano resonance. Following the procedure of analysis for two spring-mass systems [21], we can show that the power spectrum of the diaphragm displacement, $|X|^2$, near ω_2 is a Fano profile.

The solution of the displacement, *X*, for the coupling system is

$$X = P_0 \frac{(-\omega^2 + i\gamma_e\omega + \omega_e^2)}{(-\omega^2 + i\gamma_m\omega + \omega_m^2)(-\omega^2 + i\gamma_e\omega + \omega_e^2) - \mu^2\omega^2} \tag{7}$$

where $\mu = Bl/\sqrt{ML}$. Note that μ has the dimension of ω. Without coupling ($\mu = 0$), the solution of displacement given in Eq. (7) is recovered. With coupling, the resonance frequency ω_{res} is found when the real part of the denominator in Eq. (7) vanishes, hence

$$(-\omega_{res}^2 + \omega_m^2)(-\omega_{res}^2 + \omega_e^2) = (\mu^2 + \gamma_e\gamma_m)\omega_{res}^2 \tag{8}$$

When ω_m and ω_e are sufficiently distinct, the two roots are near the original resonance

frequencies. The first root, ω_1, is near ω_m, and the term of ω_{res}^2 in the second bracket and the right-hand side of Eq. (8) may be approximated by ω_m^2. The same procedure is used to find the second shifted resonance ω_2 near ω_e. Hence

$$\omega_1^2 = \omega_m^2\left(1+\frac{\mu^2+\gamma_e\gamma_m}{\omega_m^2-\omega_e^2}\right) \text{ and } \omega_2^2 = \omega_e^2\left(1-\frac{\mu^2+\gamma_e\gamma_m}{\omega_m^2-\omega_e^2}\right). \tag{9}$$

The sound intensity is proportional to the power of the velocity of the radiating object, which is the diaphragm here. Therefore, we can define the "energy" of the sound wave as

$$\tilde{\epsilon} \equiv \omega^2 - \omega_2^2 = \omega^2 - \omega_e^2\left(1-\frac{\mu^2+\gamma_e\gamma_m}{\omega_e^2-\omega_m^2}\right), \tag{10}$$

which contrasts quantum mechanics where energy is described by the Einstein-Plank relation as $E = \hbar\omega$. Following the procedure of Iizawa *et al.*[21], we further define the reduced energy ϵ and Fano parameter q as follows

$$\epsilon = \frac{1}{\omega_e\gamma_m}\frac{(\omega_e^2-\omega_m^2)^2}{\omega_e^2(\mu^2+\gamma_m\gamma_e)}\tilde{\epsilon}, \tag{11}$$

$$q = q_r + iq_i = \frac{1}{\gamma_m\omega_e}(\omega_e^2-\omega_m^2) - i\frac{\gamma_e}{\gamma_m}\frac{(\omega_e^2-\omega_m^2)^2}{\omega_e^2(\mu^2+\gamma_e\gamma_m)}. \tag{12}$$

The final expression for the complex displacement is

$$X = \frac{P_0}{\omega_e^2-\omega_m^2}\frac{-(\epsilon+q)}{(\epsilon-i)}, \tag{13}$$

and its norm is

$$|X|^2 = \left(\frac{P_0}{\omega_e^2-\omega_m^2}\right)^2\frac{|\epsilon+q_r|^2+q_i^2}{\epsilon^2+1}. \tag{14}$$

When $\gamma_e/\gamma_m \ll 1$, which mean the electrical damping is much larger than the mechanical damping, the imaginary part, q_i, is close to zero which is neglected. The square of the displacement is reduced to

$$|X|^2 = \left(\frac{P_0}{\omega_e^2-\omega_m^2}\right)^2\frac{(\epsilon+q_r)^2}{\epsilon^2+1}, \tag{14}$$

which is exactly a Fano profile.

The velocity continuity condition links the incidence, reflection and the velocity of the diaphragm, namely, $P_I - P_R = i\omega\rho_0 c_0 X$, which gives the reflection coefficient as

$$\beta = \left|\frac{P_R}{P_I}\right|^2 = \left|1-\frac{2i\omega\gamma_0}{\omega_e^2-\omega_m^2}\frac{-(\epsilon+q)}{(\epsilon-i)}\right|^2, \qquad \gamma_0 = \frac{\rho_0 c_0 A}{M}, \tag{15}$$

from which the absorption coefficient can be derived: $\alpha = 1-\beta$.

By removing the rigid backing plate of the SEMD as shown in Figs. 1(a) and 1(c) in the main text, we can immediately obtain the model for sound transmission. We only need to replace the damping term from $D + \rho_0 c_0 A$ by $D + 2\rho_0 c_0 A$ to include fluid loading of non-reflecting waveguide in downstream, the lumped parameter model of sound transmission is obtained. In such case, the transmitted wave is radiated by the diaphragm to the downstream waveguide, and its intensity is $\rho_0 c_0 |v|^2$. The transmission coefficient

$$r = \frac{\rho_0 c_0 |v|^2}{P_I^2/(\rho_0 c_0)} = \left(\frac{2\omega\gamma_0}{\omega_e^2 - \omega_m^2}\right)^2 \frac{(\epsilon + q_r)^2}{\epsilon^2 + 1} \tag{16}$$

is also a Fano profile.

The Fano resonance of the SEMD allows us to construct a high-Q filter for sound wave. Different from mechanical system of two resonators, the local resonance of the SEMD is contributed by electrical circuit, which allows to design Fano resonance at any desired frequency without modifying mechanical or geometry parameters. Usually when the mechanical parameters are fixed the Fano parameter q and Fano profile, as indicated by Eq. (12) and Eq. (14) (or Eq. (16)), are determined by electrical parameters. It inspires us to code the frequency of Fano resonance and digitally shape the Fano profile of the SEMD by electrical measures. Before that, the physics properties of the electromechanical coupling producing the electromechanical Fano resonance is investigated in next sub-section.

2.3. Analysis of electromechanical coupling and the Fano profile of SEMD

In this section we design a typical Fano resonance of the SEMD to show how the electromechanical coupling of the moving-coil forms the Fano resonance and changes sound reflection and absorption spectra of the SEMD.

The mechanical parameters of the SEMD are M = 4 g, K = 14.21 kN/m and $D = 0.5\rho_0 c_0$, respectively. The mechanical parameters give a resonance frequency of the diaphragm of $f_m = 300$ Hz. The parameters for the R-L-C shunt circuit are R = 0.2 Ω, L = 0.1 H and C = 517 nF, respectively, with the inherent coil resistance and inductance included in R and L. It gives the frequency of the electrical resonance as $f_e = 700$ Hz. The cross-section area of the waveguide is A = 0.08 m × 0.08 m and the force factor the moving-coil is $Bl = 4.6$ T · m. Fig. 3 shows the calculations results.

The two original resonance frequencies $f_m = 300$ Hz and $f_e = 700$ Hz are shifted to

f_1 =299.5 Hz and f_2 = 701.1 Hz, by the electromechanical coupling, respectively. The latter frequency shift ($f_e \rightarrow f_2$) are marked in zoom-in windows of Figs. 3(a) and 3(b), which show asymmetrical profiles. A drastically transition of the absorption and reflection is present near f_2. The reflection coefficient at f_2 drops from 82% to 0.014% merely within 2 Hz, giving a maximum ER over 6000. The absorption coefficient experiences a transition from 8% to unity within the same frequency range.

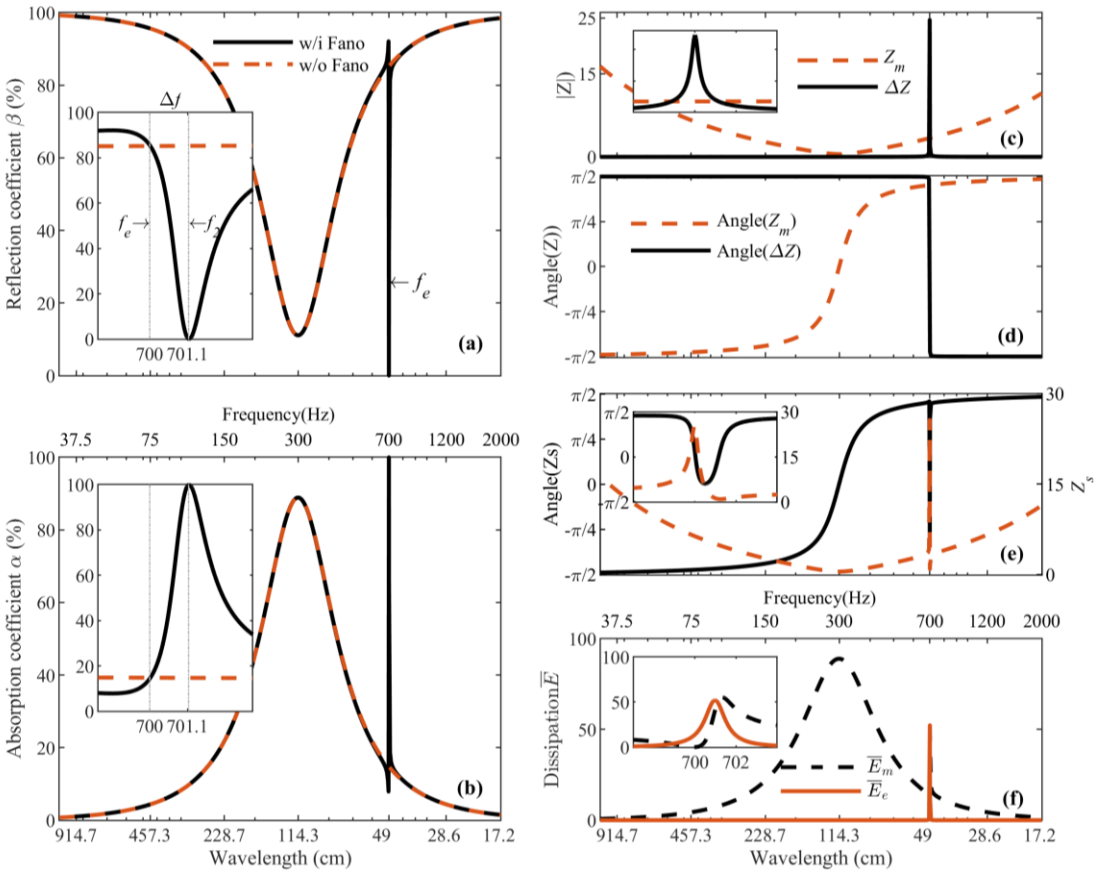

Figure 3: Calculation results of acoustic Fano resonance of the SEMD. (a-b) Reflection and absorption spectra of the SEMD with (marked as "Local") and without (marked as "Background") coupling to the local electrical mode. Details near the frequency of the local mode are shown in the same figure. (c-d) Magnitudes and phases of the acoustic impedance (Z_m) of the suspended diaphragm and EIA impedance (ΔZ). (e) Magnitude and phase of the overall acoustic impedance of the SEMD. (f) Normalized electrical dissipation ($\bar{E}_e$) and mechanical dissipation ($\bar{E}_m$). (a)-(f) share the same x-axis. Both frequency and wavelength axes are shown.

The partial spectra of the electromechanical coupling are shown in Figs. 3(c-f). The magnitude of the EIA impedance, $|\Delta Z| = |(Bl)^2/Z_e|$, is symmetrical about f_e as Fig. 3(d) shows. Its phase jumps from $\pi/2$ to $-\pi/2$ when the frequency increases from f_e^- to f_e^+, where f_e^- is in the left neighborhood of f_e and f_e^+ is in the right neighborhood. The addition of the mechanical impedance of the diaphragm (Z_m) and the EIA impedance (ΔZ) forms the overall impedance of the SEMD. Therefore, the EIA impedance increases the impedance at f_e^- and cancels it at f_e^+, which gives an asymmetrical profile of overall acoustic impedance near f_e, shown in Fig 3(e). We can also explain the asymmetrical shape through reviewing the driving force. First, a constant force exerted by the incident sound wave gives a symmetrical spectrum of the displacement (or velocity) response of the diaphragm. Due to the electromechanical coupling, an additional Lorentz force is induced, whose phase is determined by the electrical circuit which experiences a shift of π around f_e. The overall driving force of the diaphragm, therefore, is reduced at f_e^- and enhanced at f_e^+, which leads to asymmetrical spectra of the acoustic impedance, displacement, sound reflection and absorption.

Results in Fig. 3 shows that the magnitude and phase of the overall acoustic impedance (Z_s) near f_e = 700 Hz are dominated by the electrical elements. By programing the circuit resonance, a sharp and asymmetrical absorption peak and reflection dip is obtained at f_2 in the vicinity of f_e. This feature allows us to program the profile of the absorption and reflection spectra near the frequency of f_e through setting the circuit parameters to obtain a high-Q filter. Furthermore, the electrical resonance frequency, f_e, is determined by the serial capacitance (C) and inductance (L). Theoretically, we can realize a desired Fano profile at any designated frequency.

Above analysis, which shows the Fano profile is governed by the electrical parameters and elaborates the mechanism of coupling mechanical and electrical resonances to form Fano resonance for revising the reflection and absorption spectra of the SEMD. In the following section, the dependence of the Fano profile on the electrical parameters are investigated and the programable selective filter for sound wave is demonstrated in calculations.

3. Parametrical analysis of circuit effects on the Fano profile

In this section, we illustrate programing the Fano profile of the SEMD to obtain a high-Q

acoustics filter through tuning the circuit parameters. The Fano profile has three important indices, the frequency, Q factor and extinction ratio (ER). Q factor describes the bandwidth of the Fano profile. A higher Q factor means a narrower bandwidth of the Fano profile and the SEMD is more selective around the frequency of the Fano resonance. ER is also known as switching ratio or modulation depth, representing the difference between the original spectrum and the interfered spectrum. A higher ER indicates the stronger ability of changing the sound reflection spectrum of the SEMD by the circuit. Tables shows the mechanical, electrical, and coupling parameters for following analysis.

Table 1: Parameters for analysis of circuit effects on Fano profile and sound absorption/reflection spectra of the SEMD.

Mechanical parameters and coupling parameters					
M (g)	K(kN/m)	$D(\rho_0 c_0)$	f_m	A(cm^2)	Bl (T·m)
4	14.21	0.5	300	64	4.6
Electrical parameters					
	C (uF)	L (mH)	f_e (Hz)	R	
Set 1	50	22.52	150	0.1	
	50	0.352	1200	0.1	
Set 2	5	225.2	150	0.1	
	5	3.52	1200	0.1	
Set 3	61.84	100	64	swept	
Set 4	0.1546	100	1280	swept	
Set 5	2.81	100	300	swept	
Set 6	0.5166	100	700	swept	

The mechanical and coupling parameters are kept the same as listed in the caption of Fig. 3. In the mechanical parameters, K = 14.21 kN/m means the equivalent thickness of the SEMD is $Th = \rho c^2 A/K \approx 68.8$ mm, regarding the temperature is 21°. Six sets of circuit parameters are designed as listed in Table 1. The first two sets parameters are to investigate effects of inductance on the frequency of the Fano resonance and the Q factor. Set-3 to Set-5 are to study programing frequency of Fano resonance and Q factor by tuning capacitance and resistance. The capacitance value varies in these 3 sets of circuit parameters to shift the frequency of Fano resonance, and each set of the circuit parameters sweeps the resistance to change the Fano

profile of the sound absorption spectrum and Q factor. The last set of the circuit parameters are to investigate relations between effective resistance and extinction ratio, which shows that the circuit can total change the sound absorption state of the SEMD.

Through the parametrical investigations, we hope to find out the programing spaces of the electromechanical Fano resonance and finally realize a high-Q acoustic filter by SEMD for picking up or eliminating the sound energy at local frequencies without interfering the background propagation.

3.1 Circuit effects on Fano resonance frequency and Q factor

The calculation results using parameters of Set-1 and Set-2 are shown in Fig. 4. As shown in Fig. 4(a)，by tuning the inductance to 0.352 mH and 25.52 mH, the electrical resonance frequency is set to $f_{e1} = 150$ Hz and $f_{e2} = 1200$ Hz，respectively. Around the two electrical resonance frequencies are the new resonance frequency f_2 which is the frequency of Fano resonance and the asymmetrical sound absorption spectrum profiles present.

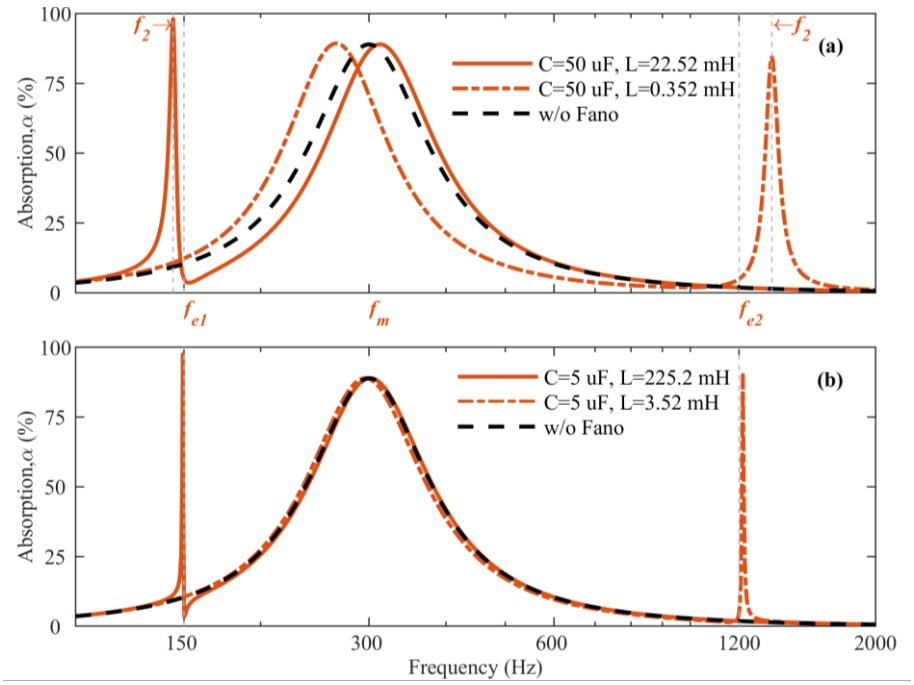

Fig. 4: Investigation of inductance effects on the frequency and Q factor of electromechanical Fano resonance and the sound absorption spectrum of the SEMD. (a) Absorption spectra obtained by parameters of Set-1. (a) Absorption spectra obtained by parameters of Set-2.

When the capacitance is tuned to 1/10 and the inductance is adjusted to 10 times of those used for Fig. 4(a), respectively, we obtain calculated sound absorption spectra shown in Fig. 4(b). The electrical resonance frequencies keep. Two points should be noted in the figure. First, the discrepancy between f_2 and f_e in Fig. 4(b) are smaller than that shown in Fig. 4(a). It can be explained by Eq. (9), which shows that $\gamma_e = L/R$ determines the difference between f_2 and f_e. Second, the absorption peaks of f_2 in Fig. 4(b) are much sharper than that in Fig. 4(a), which means that a smaller capacitance and larger inductance will give a high quality Fano resonance. It is because that a smaller capacitance and a larger inductance will introduce a more rapid phase shift of the EIA impedance around f_e,, which results in the phase of the impedance of SEMD approaching and departing zero in a narrow band width as shown in Fig. 3(d) and Fig. 3(e), while a zero phase means a resonance and a sound absorption peak of SEMD. The conclusion is that a large inductance, which means a small capacitance, is one of the keys to achieve a high Q acoustic filter by SEMD around desired f_2.

In the following, we use electrical parameters of in Set-3 to Set-5 in Table 1 to study tuning the Fano resonance and sound absorption/reflection spectrum of the SEMD. Each set of circuit parameters has a different effective capacitance and a constant inductance of 100 mH, while the effective resistance is swept for the same parameter set.

Fig. 5 shows the calculation results obtained by using electrical parameters of Set 3 in Table 1. The resistance is swept from 1 mΩ to 4096 mΩ to obtain a set of absorption spectra of the SEMD. The waterfall plots of the spectra are shown in Fig. 5(a). There are two absorption peaks for each absorption spectrum. The frequencies of the peaks are $f_1 \approx 302.3$ Hz and $f_2 \approx 63.5$ Hz. f_1 is the new resonance frequency shifted from $f_m = 300$ Hz and $f_2$is the frequency of Fano resonance shifted from $f_e = 64$ Hz.

Fig. 5(b) shows the cross line of f_2 plane and the waterfall, which is the curve of sound absorption coefficient of the SEMD at f_2 against the effective resistance(R). With a suitable resistance, which is R = 25.99 mΩ as marked in Fig. 5(b) by the solid cycle, the impedance matching condition is realized, and a perfect sound absorption is achieved at f_2. The Q factor of the Fano profile against the R is also plotted in the same figure, which monotonically increases with the decreasing of the resistance. It's because that the effective resistance

determines the coupling efficiency, $(Bl)^2/R$. We can also view it through phase shift of the EIA impedance. With a smaller effective resistance, it has a more rapid phase shift around f_e, which results in a narrower band width of the absorption peak. For R = 25.99 mΩ, the Q factor is 396, which means that a half bandwidth of $\Delta f = f_2/\mathrm{Q} \approx 0.16$ Hz.

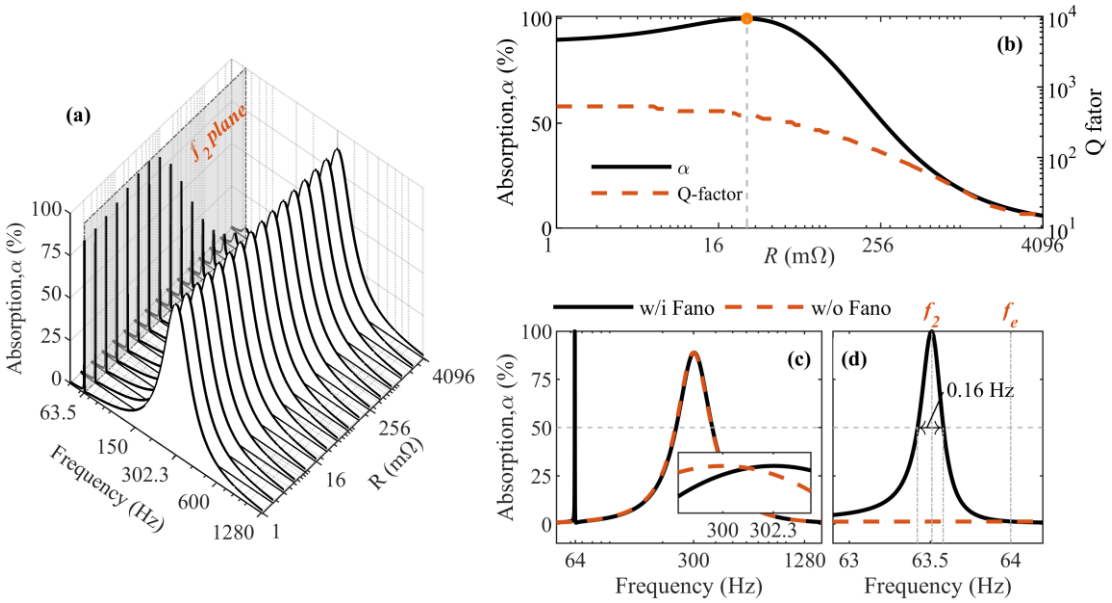

Fig. 5: Sound absorption spectra of the SEMD with Fano profile around $f_e = 64$ Hz obtained by parameters of Set-3 in Table 1. (a) Waterfall plot of sound absorption spectra of the SEMD with different effective electrical resistance. (b) Peak sound absorption coefficient of the SEMD at f_2 (solid curve, left axis) and Q factor (dash curve, right-axis) of absorption peak while varying the electrical resistance. R = 25.99 mΩ leads to a perfect sound absorption at f_2 as the solid cycle marks. (c) Sound absorption spectra with (solid curve) and without (dash curve) Fano profile for R = 25.99 mΩ. (d) Zoom-in view of the sound absorption peak around f_2.

The sound absorption spectrum for R = 25.99 mΩ is shown in Fig. 5(c) and the absorption spectrum for the diaphragm without Fano resonance (no coupling) is also plotted for comparison. The zoom-in view around f_m = 300 Hz is shown in the same figure which illustrates the resonance frequency shifting from $f_m = 300$ Hz to $f_1 = 302.3$ Hz. The spectrum with Fano profile has a very narrow and sharp absorption peak at f_2. The zoom-in view of the absorption peak raised by the Fano profile is shown in Fig. 5(d), which clearly shows its

asymmetrical line shape and the frequency shifting from $f_e = 64$ Hz to $f_2 = 63.5$ Hz. The half bandwidth, $\Delta f = 0.16$ Hz, is marked in the figure.

In a summary, by setting the electrical resonance frequency to $f_e = 64$ Hz, we obtain a high quality Fano resonance at $f_2 = 63.5$ Hz near f_e, which enables the SEMD to filter the reflection wave in a very narrow bandwidth.

It's interesting to find that the frequency of the Fano resonance, which is also the new acoustic resonance, can be fast configured by the electrical circuit. This unique property allows us to program the acoustic filter in a digital manner, regardless of the complication and inaccuracy of mechanical and geometrical designs. In what follows, we show high frequency results with circuit parameters of Set-4 in Table 1, which gives an electrical resonance frequency of $f_e = 1280$ Hz. The results are shown in Fig. 6.

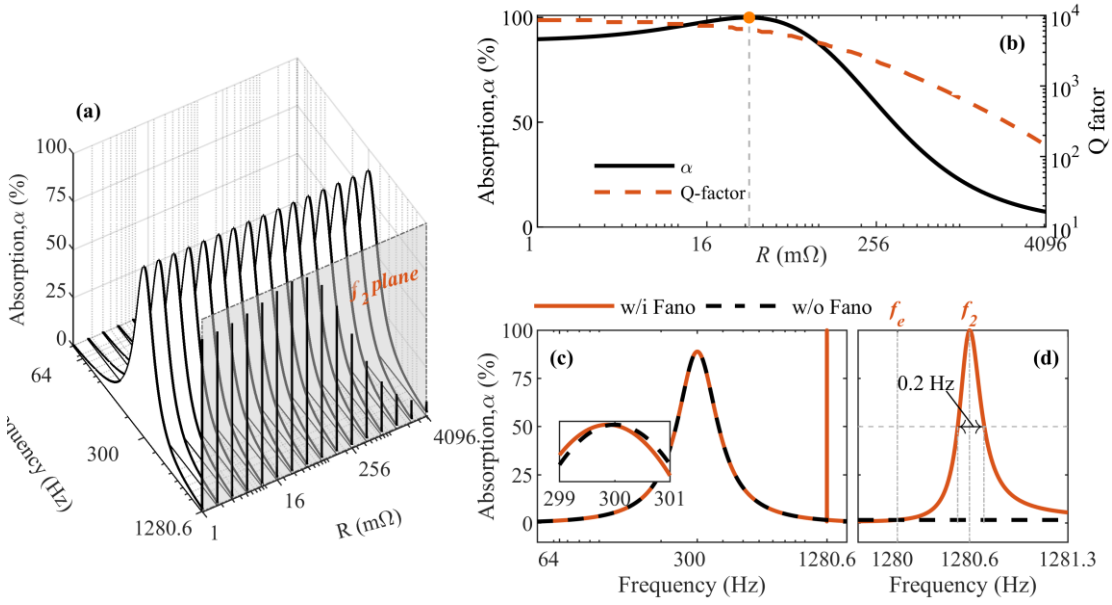

Fig. 6: Sound absorption spectra of the SEMD with Fano profile around $f_e = 1280$ Hz obtained by parameters of Set-4 in Table 1. (a) Waterfall plot of sound absorption spectra of the SEMD with different effective electrical resistance. The Fano profile is in the vicinity of f_2 plane and f_2 = 1280.6 Hz. (b) Peak sound absorption coefficient of the SEMD at f_2 (solid curve) and Q factor (dash curve) of the absorption peak while varying the electrical resistance. R = 32.0 mΩ leads to perfect sound absorption at f_2 as marked by the solid cycle. (c) Sound absorption spectra with (solid curve) and without Fano profile (dash curve). (d) Zoom-in view of the sound absorption peak raised by the Fano resonance.

Fig. 6(a) shows the waterfall plots of the calculation results for f_e= 1280 Hz. The frequency of the Fano resonance is f_2=1280.6 Hz, at which sound absorption peaks present. Fig. 5(b) shows the sound absorption coefficient against effective resistance, and the Q factor is also plotted in the same figure. Perfect sound absorption is achieved for R=32 mΩ, marked by a solid cycle. The corresponding Q factor is 6403, which means the half bandwidth of the absorption peak around f_2 is $\Delta f = 1280.6/6403 \approx 0.20$ Hz. Therefore, a high Q filter for the reflection sound wave is achieved. Fig. 6(c) shows the sound absorption spectrum for R = 32 mΩ. The zoom-in view around f_m= 300 Hz shows that the mechanical resonance frequency is shifted little due to the electrical resonance is far away from the mechanical resonance in frequency. Fig. 6(d) shows the zoom-in view around f_2=1280.6. The half bandwidth and the frequency shift are marked.

Results in Fig. 5 and Fig 6 show that, by tuning the capacitance and resistance, the frequency of the perfect sound absorption raised by the electromechanical Fano resonance can be programed digitally from 64 Hz to 1280 Hz, which is over 4 octaves. It's also feasible to alter the frequency of the Fano resonance through tuning the inductance, however, the inductance should be large enough to promise a high Q factor. Ideally, we can realize the electromechanical Fano resonance and a perfect sound absorption at any desired frequency by programming the R-L-C circuit, as long as the resistance can be tuned to sufficiently small [58].

A special case is that the electrical resonance frequency coincides with the mechanical resonance frequency, namely, $f_e = f_m$. In this case, equations and analysis in section 2.2 are invalid. However, we can quickly find that there will be two new resonances presents in the left and right vicinities of f_m through revisiting the analysis of Fig. 3(d) and Fig. 3(e). Fig. 7 shows the calculations results for $f_e = f_m$ using electrical circuit parameters of Set-6 in Table 1.

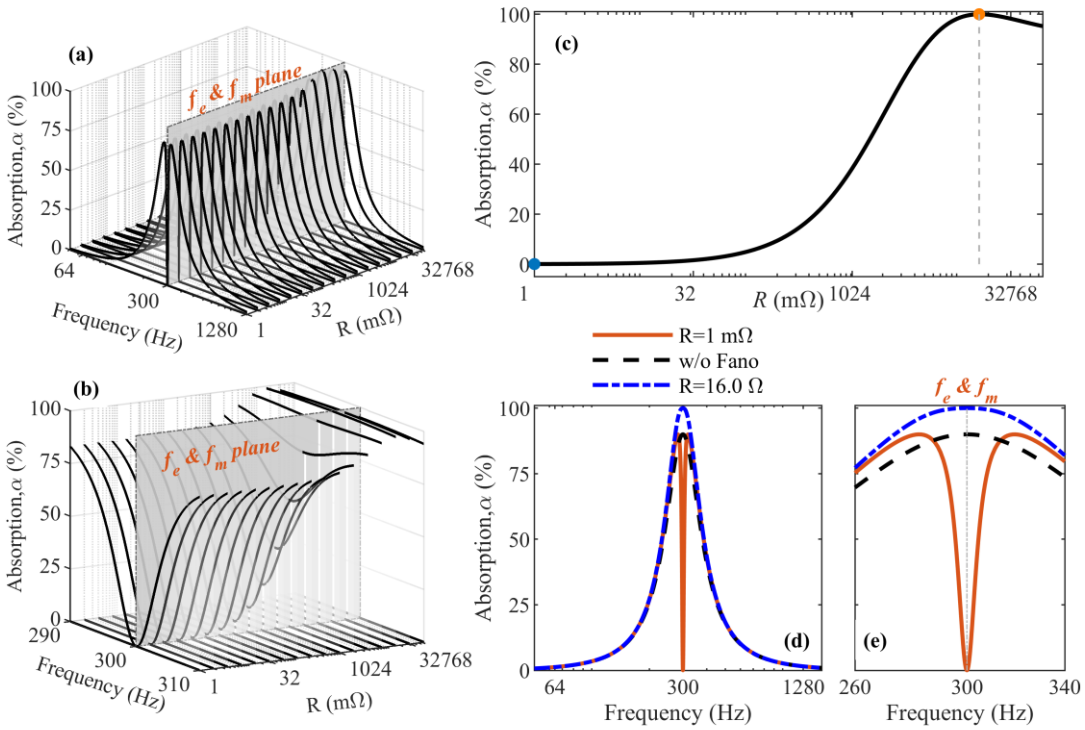

Fig. 7: Sound absorption spectra of the SEMD with Fano profile around f_e = f_m = 300 Hz. (a) Waterfall plot of sound absorption spectra of the SEMD with different effective electrical resistance. In this case $f_e = f_m$ 300 Hz. (b) Zoom-in view of (a) around 300 Hz. (c) Sound absorption coefficient at 300 Hz of the SEMD against the electrical resistance *R*. Two critical points, *R* = 1 mΩ and *R* = 16.0 Ω, are marked by solid circles, at which total sound reflection and absorption are achieved, respectively. (d) Sound absorption spectra for *R* = 1 mΩ (solid curve), *R* = 16.0 Ω (dash dot curve) and without Fano profile (dash curve). (e) Zoom in view of (d) around 300 Hz.

Fig. 7(a) shows the waterfall plot of sound absorption spectra and Fig. 7(b) shows its zoom-in view around $f_m = f_e$ = 300 Hz, which is a canyon shape. The dependency of sound absorption coefficient on the effective resistance *R* is shown in Fig. 7(c). It shows that, with the increasing of the resistance, the sound absorption coefficient achieves 100% for *R* = 16.0 Ω and drops above that. When we want to realize perfect sound absorption at the frequency that further from f_m = 300 Hz, such as around 64 Hz and 1280 Hz as Fig. 5 and Fig 6 show, it requires the circuit to induce a huge out-of-phase EIA reactance to neutralize the mechanical reactance to achieve impedance matching condition. To achieve it, as Eq. (3) indicates, the serial resistance

needs to be sufficiently small. In contrast, the original reactance of the diaphragm is already zero at f_m = 300 Hz. To attribute perfect sound absorption to SEMD at this frequency, it only needs to match its damping to that of air. The original damping of the diaphragm is $0.5\rho_0 c_0 A$, meaning an additional damping of $0.5\rho_0 c_0 A$ is required. Considering the EIA damping is $(Bl)^2/R$, it hence requires the effective serial resistance $R = (Bl)^2/(0.5\rho_0 c_0 A)$ = 16.0 Ω to match the impedance. When the electrical resistance *R* is very small, the circuit is close to short states and EIA damping, $(Bl)^2/R$, is huge which leads to even total sound absorption at $f_m =$ 300 Hz; When the electrical resistance *R* approaches infinity, the circuit is effectively disconnected, and the sound absorption coefficient is reduced to that of the diaphragm itself.

The full sound absorption spectra of the SEMD for *R* = 1 mΩ, *R* = 16.0 Ω and *R* = 1 ∞ (without Fano resonance) are shown in Fig. 7(d) and the zoom-in view around $f_m = 300$ Hz are shown in Fig. 7(e). When *R* = 1 mΩ, total reflection happens at $f_m = 300$ Hz, which splits the sound absorption spectrum into two-peaks pattern. As explained above, it's due to the huge EIA damping induced by the small effective resistance. We can also explain this phenomenon by the mechanism of Rabi splitting [59,60]. A tiny effective resistance *R* means a strong electrotechnical coupling. At $f_e = f_m$ = 300 Hz, if the mechanical damping of the SEMD is sufficient low, which is the case in this calculation, a small incident sound wave will raise a significant magnitude of vibration velocity of the diaphragm. It further induces a large voltage across the coil that leads to huge electrical current in the circuit and results in a very strong anti-phase Lorentz force on the coil attached to the diaphragm. This Lorentz force counteracts the driving force caused by the incident sound, which reduces the net force applied on the diaphragm to zero, therefore, the diaphragm keeps tiny movement, and the total sound reflection is approached. The overall effect, in the angle of acoustics impedance, is that the circuit induces a huge EIA damping to the SEMD due to the strong coupling, which is $8006Z_0$ for *R* = 1 mΩ. If the SEMD-duct system is conservative, the energy will be exchanged between the acoustics resonance and electrical resonance coherently. Similar to the atom-cavity system with strong coupling [59,60], the diaphragm-circuit system with a strong electromechanical coupling forms the Rabi oscillator, which has a slitted transmission spectrum.

A significant result of above analysis is that, by only tuning the effective resistance, the

SEMD can either totally reflect or absorb sound wave at $f_e = f_m = 300$ Hz. This is a switching effect for acoustic wave and the diaphragm can be called as binary materials. It is important for constructing temporally modulated materials or structures used for modulating sound wave, mimicking the electronic switch ratifying the electrical current, marching a solid step to our vision of digitally control of sound waves.

3.2 Circuit effects on extinction ratio

In former section we show that the circuit induced electromechanical Fano resonance can effectively change the sound absorption and reflection spectrum of the SEMD. In this section we investigate the extent of the sound reflection and absorption spectrum altered by the electromechanical coupling, indexed by extinction ratio (ER). ER is a terminology from optical telecommunication, in which the output power levels with light source switched on and off represent "1" and "0", respectively. The ratio of the two output levels therefore is called extinction ratio. A higher ER indicates that there is a sufficient power difference between the digital "1" and "0". By investigating the ER, we can find out the parameter space for programing the magnitude of selective filtering by the SEMD. In this demonstration, electrical parameters in Set 4 of Table 1 are used which gives f_e = 700 Hz.

Fig. 8(a) shows waterfall plot of ER spectra for different effective resistance. It's demonstrated that ER is distinguished in the vicinity of f_2, meaning the effect of the electromechanical coupling of mechanical and electrical resonances is locally effective. Fig. 8(b) shows the zoom-in view ER spectra around f_2, which further illustrates that the electrical resonance only changes the reflectance in the vicinity of f_2. The maximum ER is as high as 61 dB when R =139.29 mΩ as shown in Fig. 8(c), which means by switching on and off the circuit, the reflectance changes by 10^6 times. In fact, the maximum ER can be much higher if we use a smaller step to sweep the effective resistance in the calculations. Fig. 8(d) shows the reflection spectrum for R =139.29 mΩ and the spectrum without Fano profile is plotted for comparison. Fig. 8(e) shows the details of the spectrum around $f_2 = 701.2$.

ER also represents the modulation depth, which is one of the most important fundamental parameters for modulator. Recently, both the research topics of time-crystal and temporal metamaterials are chasing high modulation depth to construct linear time-varying materials for

exploring new physics in time dimension by temporal modulating materials. The SEMD with extremely high ER, as shown by current calculations, therefore, is a superior candidate for constructing time-varying materials or structures.

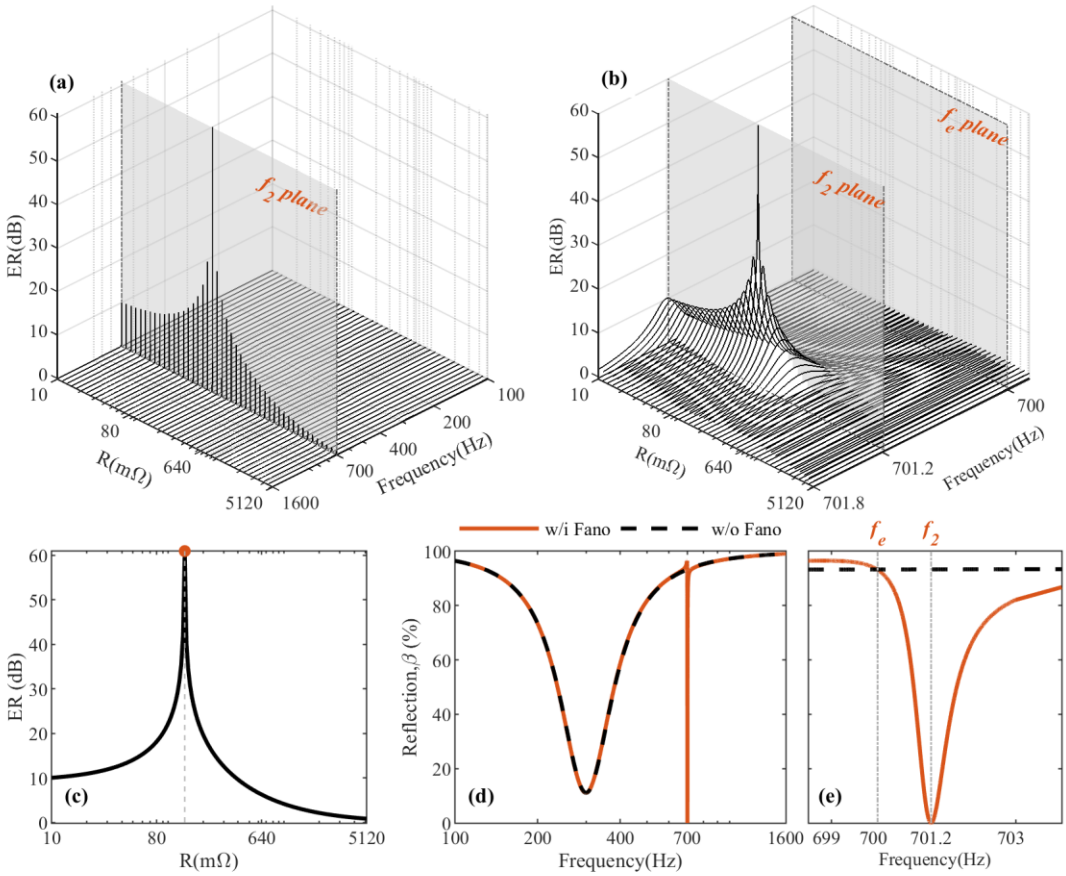

Fig. 8: Programing the extinction ratio (ER) of reflectance for $f_e = 700$ Hz. (a) Waterfall plot of ER spectra with different effective resistance. (b) Zoom-in view of (a) around f_e. (c) ER at $f_2 = 701.2$ Hz against effective resistance. ER achieved maximum for R = 139.29 mΩ Ω. (d) Reflection spectrum for R = 139.29 mΩ (solid curve). The spectrum without Fano profile (dash curve) is also plotted for comparison. (e) Zoom-in view of the reflection spectra around $f_2 = 701.2$ Hz.

4. Experiments

4.1 Experimental setup

Experimental verification is conducted in an impedance tube with a cross section of 8 cm by 8 cm as shown in Fig. 9 (a). Its cut-off frequency is $f_c \approx 2144$ Hz, below which only plane propagation is allowed. The impedance tube is with a sound source forming its left-end and the

SEMD forming the right-end. The sound source at left end radiates a white noise with a frequency range of [20 Hz ~ 2000 Hz].

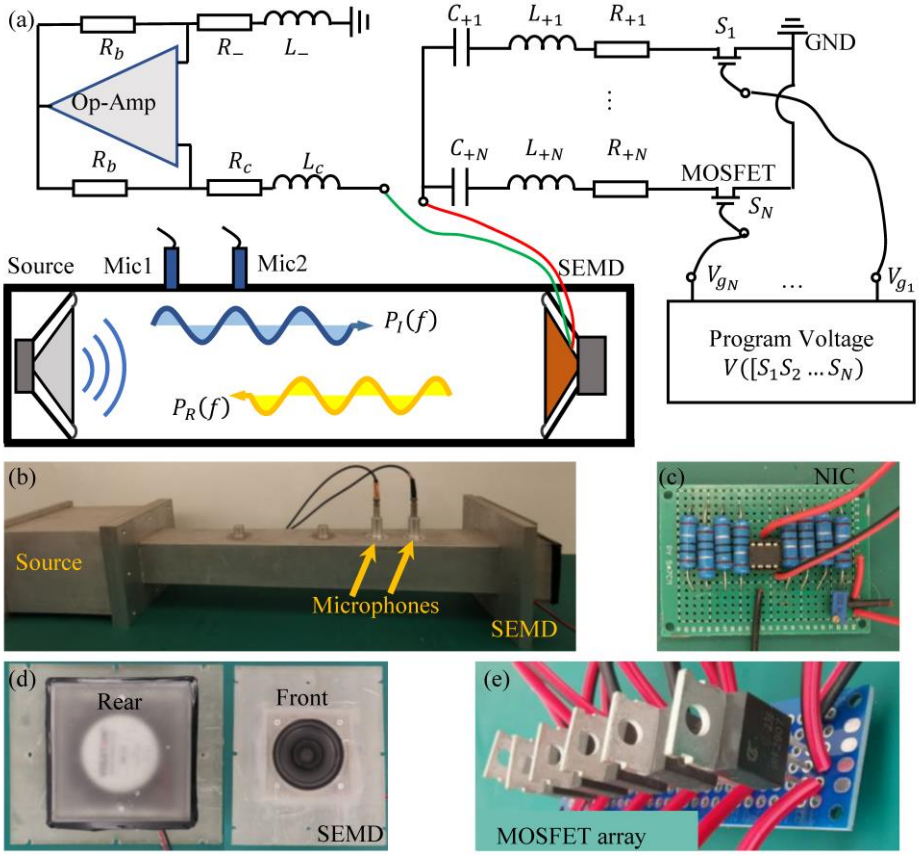

Fig. 9: Experimental setup to investigate electromechanical Fano resonance of the SEMD. (a) Schematic o the SEMD and the measurement impedance tube. A negative impedance converter, which is an operational amplifier (marked as Op-Amp) circuit, is used to introduce negative resistance (R_-) and inductance (L_-) to neutralize the resistance (R_c) and inductance (L_c), respectively. (b) Photograph of the impedance tube with SEMD forming it right end. (c) Photograph of the negative impedance converter. (d) Front view and rear view of the SEMD. (e) The MOSFET array.

Due to the reflection by the SEMD at the right-end, the left and right travelling waves are form, which are denoted by $P_I(f)$ and $P_R(f)$ in Fig. 9, respectively, and the superposition of $P_I(f)$ and $P_R(f)$ forms standing waves in the impedance tube. Two microphones (BSWA MPA253 type) with 8 cm distance are flushed mounted on the tube wall to collect pressure data, which are calibrated by swapping method [61,62]. Data acquisition system from National

Instrument are used for voltage generation, collection and power supply of microphones. The system including one NI 9232 input module, three NI 9263 output modules, and NI 9174 chassis box. Microphones are directly connected to NI 9232 module, which can supply a constant current power. NI 9263 module is used for signal generation and supplying the programing voltages for MOSFET arrays. A well-known transfer-function method [61,62] is used to decompose the standing wave in the tube using the pressure data collected by the two microphones, with which the absorption and reflection spectra are obtained.

The SEMD sample is shown in Fig. 9(d), which is formed by sealing a commercially available loudspeaker in a 3D printed box. Both glue sealing and adhesive tape are used to promise little acoustics leakages of sound from the box, which is detrimental to the accuracy of low frequency measurement. The coil resistance and inductance are denoted by R_c and L_c respectively. In experiments, we use a commercial moving-coil loudspeaker to realize the SEMD, for which R_c is normally 4 Ω or 8 Ω and the inductance is about 0.2 mH ~ 1 mH. A negative impedance converter is used to mitigate the coil resistance and inductance.

A passive circuit with six branches is connect to another termination of the moving-coil and each branch of the circuit is switched on and off by the switching voltage $[V_{S_1}, V_{S_2} \ldots V_{S_N}]$. $V_{S_n} > V_{\text{threhold}}$ activating n^{th} circuit branch and the state of n^{th} MOSFET turning to be $S_n = 1$. When the n^{th} circuit branch is switched on, the effective electrical impedance of the circuit are

$$R_n = R_{+n} + R_c - R_-,\ L_n = L_{+n} + L_c - L_-\ , C_n = C_{+n}. \tag{17}$$

To guarantee the stability of the SEMD, R_n, L_n and C_n should be kept positive. When overall resistance R_n is small, such as $0 < R_n < 0.1$ Ω, it's difficult to tune it precisely due to the nonlinear resistance raised by iron-loss of the speaker. When $R_n > 0.1$ Ω, it is relatively easy to tune it to a targeted value with a small relative error. Nevertheless, the tuning of R_n have little effects on the local resonance, which is determined by the effective capacitance and inductance. The inductances, both the coil inductance and additional inductance of the wired inductor in the shunt circuit, are $\chi_L = \omega^n L$, and n value depends on the core materials. In this study, the *n* values for coil inductance and wired inductor are different, which leads to that we can only partially cancel the coil inductance. But fortunately, we don't need a very small effective inductance in present study.

To reveal mechanisms of the electromechanical Fano resonance, we only allow one circuit branch being activated. There are 7 states for the SEMD for current studies including the original state without shunt. The effective circuit parameters of each state are listed following table. Mechanical and coupling parameters are the same as those used in analytical calculation.

Table 2. Circuit parameters for experiments

States	R	L (mF)	C (uF)	f_e
$S_0 = 1$	∞	-	-	-
$S_1 = 1$	0.05	2.34	5.00	1472.3
$S_2 = 1$	0.43	51.23	2.12	484.0
$S_3 = 1$	0.21	19.47	47.02	166.4
$S_4 = 1$	0.011	51.23	2.12	484.0
$S_5 = 1$	2.02	51.23	2.12	484.0
$S_6 = 1$	5.17	51.23	2.12	484.0

The states of $S_{1,2,3} = 1$ are for programing frequency of perfect sound absorption coefficient raised by the Fano profile and the states of $S_{3,4,6} = 1$ are for programing the extinction ratio of the Fano profile.

4.2 Experimental results

The results of programing the frequency of perfect sound absorption are shown in Fig. 9(a), in which both wavelength axis (bottom) and frequency axis (top) are plotted. By coding $S_1 = 1$, $S_2 = 1$ and $S_3 = 1$ to activate the corresponding circuit branch, we successfully program the frequency of perfect sound absorption to 157.5 Hz, 484.5 Hz and 1486.75 Hz, respectively. The sound absorption coefficients at these frequencies are marked in figure, which are 99.43%, 99.19% and 98.75%, and these frequencies correspond to wavelengths of 23.1 cm, 70.8 cm and 217.8 cm, respectively. Compared to the effective thickness of the SEMD of 6.88 cm, the wavelengths to thickness ratios are 3.35, 8.53 and 31.65, respectively. For $S_1 = 1$, extremely deep sub-wavelength sound absorption is achieved. The Q factors of the three absorption peaks for $S_1 = 1$, $S_2 = 1$ and $S_3 = 1$ are 21, 64.6 and 145, which means the half bandwidth is 7.5 Hz,

7.5 Hz and 10.25 Hz, respectively.

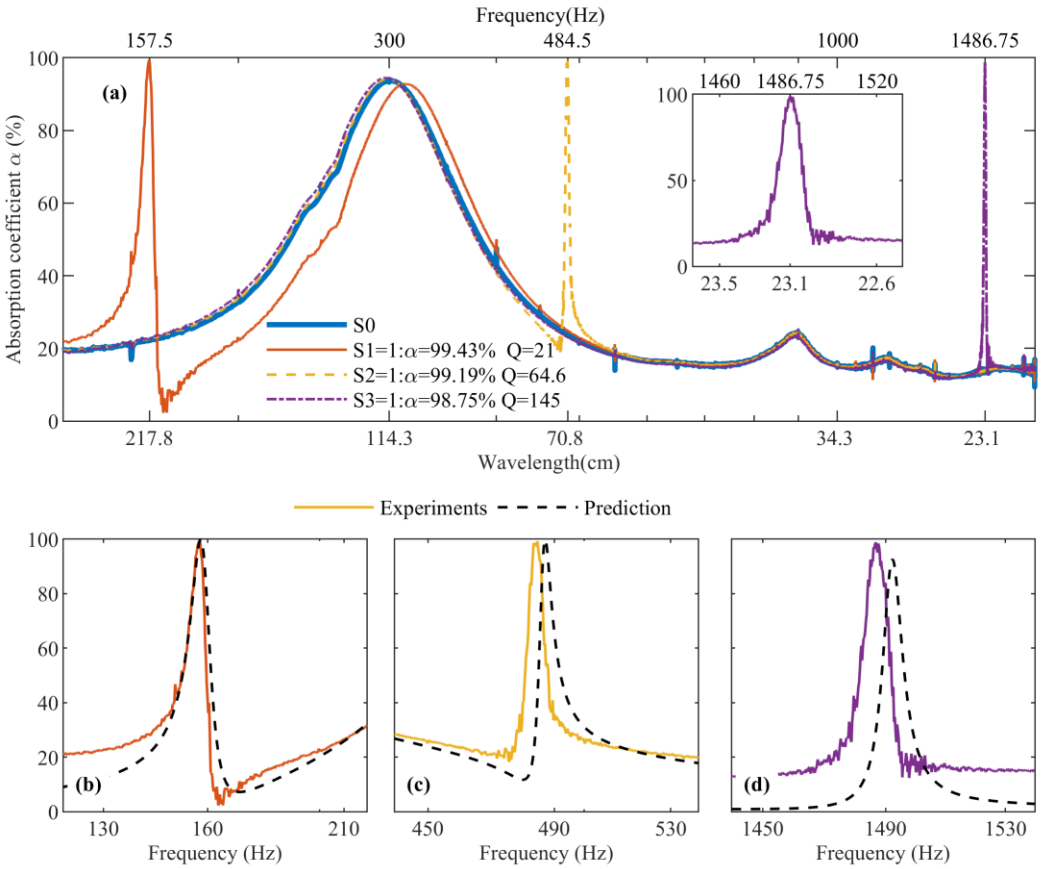

Fig. 10: Experimental verification of programming frequency of perfect sound absorption. (a) Spectra for $S_{0,1,2,3} = 1$. (b)-(d) Comparisons of experimental (solid curve) and predicted (dash) results for $S_{1,2,3} = 1$.

The predictions are shown in Fig. 10(b)~Fig. 10(d) which shows good agreements with the experimental curves. The discrepancies are caused by the nonlinearity of the wired inductor.

In current results, the programable frequency range is 157.5 Hz to 1486.75 Hz, which is 3.24 octaves. Ideally, by finer tuning to further reduce the electrical resistance, we can realize perfect sound absorption at any desired frequency. In practice, however, despite the inherent resistance of the coil, the magnetic vortex in the iron core also induces parasitic iron loss. This not only further increases the effective resistance of the circuit, but also brings in nonlinearity in its frequency response, complicating the tuning. The Q value can also be further increased by using much larger inductance, but which will also induce significant nonlinearity. It's better to used simulated inductor in future work.

Fig. 11(a) shows a successful programing dip of the reflection spectrum by coding $S_4 = 1$, $S_5 = 1$ and $S_6 = 1$ to activate the corresponding circuit branch. For these three states, effective inductance and capacitance of the circuit are kept the same as listed in table 2, which give electrical resonance frequency as $f_e = 484$ Hz. The resistance varies to alter the dip and change ER. The new resonance frequency (frequency of the dip) is around $f_2 = 490$ Hz and has a slight variation with the change of effective resistance. The reflection coefficient is tuned from 76% for $S_0 = 1$ to very close to zero for the $S_1 = 1$, giving a maximum extinction ratio of ER = 752. The ER spectra, which are the ratios of the reflection spectra for $S_{1,2,3} = 1$ to that for $S_0 = 1$, are shown in Fig. 11(b). The spectra clearly show that the effect of Fano resonance is limited in a very narrow range of frequency, which is just some Hertz. The predictions of reflection spectra agree well with the experimental results as shown in Fig. 11(c) - Fig. 11(e).

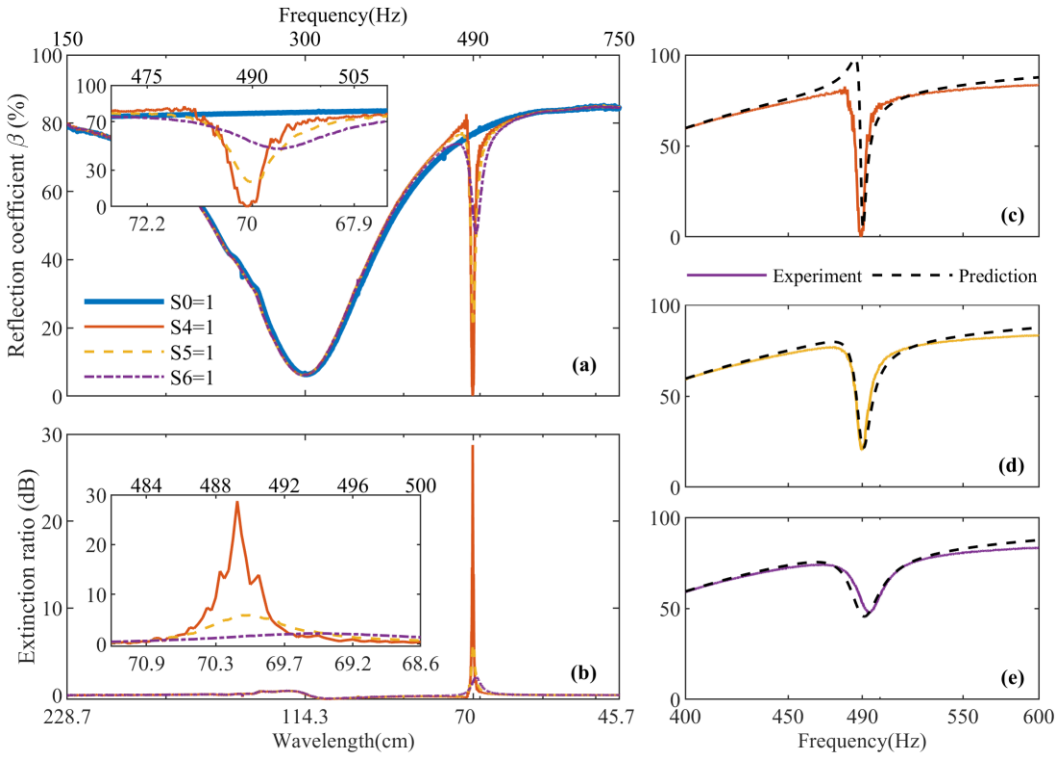

Fig. 11. Programing extinction ratio of the SEMD. (a) Reflection spectra for $S_{0,4,5,6} = 1$. Zoom-in view is plotted in the same figure. (b) Extinction spectra and the zoom-in view. (c-e) Comparison of predictions (dash curves) and experimental (solid curves) results.

5. Discussion and conclusions

To conclude, both in calculations and experiments, this work presents an electromechanical diaphragm (SEMD) with an electromechanical Fano resonance induced by the interfering the background mechanical resonance of the suspended diaphragm with an electrical resonance. The Fano profile is fully programed by activating different states of the resonant circuit through coding the voltage gating the MOSFETs, and a high-Q filter acoustics wave is realized by SEMD. Specifically, the experiments show tuning the frequency of perfect sound absorption over 3 octaves in deep subwavelength scales, the Q factor is up to 145. The high extinction ratio is up to 752 (28.76 dB), which means can totally altering the response of the mechanical diaphragm.

The theoretical predictions point out that better performance can be realized if the resistance can be further decrease in experiments, which, however, yet to be achieved by introducing sophisticated electronic circuit design. Nevertheless, this work shows that the electromechanical coupling of the coil-magnet does remove the constrains of mechanical and geometrical designs, which marching a step to the prospective of digital control of physics waves which have been well developed in structural vibration control [42,43,56,57].

In another way, the working frequency of the MOSFET is up to MHz which enable the SEMD a superior platform for studying temporal-modulated metamaterials with its features of fast switching, deep modulation depth and real-time performance. The impedances of the devices being dominated by electrical shunts results in implementing time-varying impedances for sound [44,45] and vibration control [42,43,56,57]. Many unprecedented possibilities of time-varying impedances for waves manipulations yet to be revealed and one of them, namely, converting audile sound to infrasound [44] , is realized.

.

Acknowledgements: The work is supported by a National Natural Science Foundation of China, Project No. 52105090, and a general research fund project 17210720 of the Research Grants Council of HK SAR Government.

References

[1] U. Fano, Sullo spettro di assorbimento dei gas nobili presso il limite dello spettro d'arco, Il Nuovo Cimento. 12 (1935) 154–161. https://doi.org/10.1007/BF02958288.

[2] U. Fano, G. Pupillo, A. Zannoni, W. Clark, the Arc Spectrum Limit, J. Res. Natl. Inst. Stand. Technol. 110 (2005) 583–587.

[3] U. Fano, Effects of configuration interaction on intensities and phase shifts, Physical Review. 124 (1961) 1866–1878. https://doi.org/10.1103/PhysRev.124.1866.

[4] H. Beutler, Über Absorptionsserien von Argon, Krypton und Xenon zu Termen zwischen den beiden Ionisierungsgrenzen2P32/0 und2P12/0, Zeitschrift Für Physik. 93 (1935) 177–196. https://doi.org/10.1007/BF01365116.

[5] A.E. Miroshnichenko, S. Flach, Y.S. Kivshar, Fano resonances in nanoscale structures, Rev. Mod. Phys. 82 (2010) 2257–2298. https://doi.org/10.1103/RevModPhys.82.2257.

[6] B. Luk'yanchuk, N.I. Zheludev, S.A. Maier, N.J. Halas, P. Nordlander, H. Giessen, C.T. Chong, The Fano resonance in plasmonic nanostructures and metamaterials, Nat. Mater. 9 (2010) 707–715. https://doi.org/10.1038/nmat2810.

[7] F. Zangeneh-nejad, R. Fleury, Topological Fano Resonances, Phys. Rev. Lett. 122 (2019) 14301. https://doi.org/10.1103/PhysRevLett.122.014301.

[8] A.C. Johnson, C.M. Marcus, M.P. Hanson, A.C. Gossard, Coulomb-modified Fano resonance in a one-lead quantum dot, Phys. Rev. Lett. 93 (2004) 1–4. https://doi.org/10.1103/PhysRevLett.93.106803.

[9] R.P. Madden, K. Codling, New Autoionizing Atomic Energy Levels in He, Ne, and Ar, Phys. Rev. Lett. 10 (1963) 516–518. https://doi.org/10.1103/PhysRevLett.10.516.

[10] U. FANO, J.W. COOPER, Spectral Distribution of Atomic Oscillator Strengths, Rev. Mod. Phys. 40 (1968) 441–507. https://doi.org/10.1103/RevModPhys.40.441.

[11] S. Fan, W. Suh, J.D. Joannopoulos, Temporal coupled-mode theory for the Fano resonance in optical resonators, J. Opt. Soc. Amer. A. 20 (2003) 569. https://doi.org/10.1364/josaa.20.000569.

[12] P. Fan, Z. Yu, S. Fan, M.L. Brongersma, Optical Fano resonance of an individual semiconductor nanostructure, Nat. Mater. 13 (2014) 471–475. https://doi.org/10.1038/nmat3927.

[13] R. Wang, L. Xu, J. Wang, L. Sun, Y. Jiao, Y. Meng, S. Chen, C. Chang, C. Fan, Electric Fano resonance-based terahertz metasensors, Nanoscale. 13 (2021) 18467–18472. https://doi.org/10.1039/D1NR04477J.

[14] M.F. Limonov, M. V Rybin, A.N. Poddubny, Y.S. Kivshar, Fano resonances in photonics, Nat. Photon., 11 (2017) 543-554. https://doi.org/10.1038/nphoton.2017.142.

[15] N. Liu, L. Langguth, T. Weiss, J. Kästel, M. Fleischhauer, T. Pfau, H. Giessen, Plasmonic analogue of electromagnetically induced transparency at the Drude damping limit, Nat. Mater. 8 (2009) 758–762. https://doi.org/10.1038/nmat2495.

[16] S. Zhang, D.A. Genov, Y. Wang, M. Liu, X. Zhang, Plasmon-induced transparency in metamaterials, Phys. Rev. Lett. 101 (2008) 1–4. https://doi.org/10.1103/PhysRevLett.101.047401.

[17] Y. Shuai, D. Zhao, Z. Tian, J.-H. Seo, D. V. Plant, Z. Ma, S. Fan, W. Zhou, Double-layer Fano resonance photonic crystal filters, Opt. Express. 21 (2013) 24582.

https://doi.org/10.1364/oe.21.024582.
[18] C. Wu, A.B. Khanikaev, G. Shvets, Broadband Slow Light Metamaterial Based on a Double-Continuum Fano Resonance, Phys. Rev. Lett. 106 (2011) 107403. https://doi.org/10.1103/PhysRevLett.106.107403.
[19] Y.S. Joe, A.M. Satanin, C.S. Kim, Classical analogy of Fano resonances, (2006). https://doi.org/10.1088/0031-8949/74/2/020.
[20] S. Hein, W. Koch, L. Nannen, Fano resonances in acoustics, J. Fluid. Mech. 664 (2010) 238–264. https://doi.org/10.1017/S0022112010003757.
[21] M. Iizawa, S. Kosugi, F. Koike, Y. Azuma, The quantum and classical Fano parameter q, Phys. Scr. 96 (2021). https://doi.org/10.1088/1402-4896/abe580.
[22] S. Hein, W. Koch, L. Nannen, Trapped modes and Fano resonances in two-dimensional acoustical duct–cavity systems, J. Fluid. Mech. 692 (2012) 257–287. https://doi.org/10.1017/jfm.2011.509.
[23] C.W. Hsu, B. Zhen, A.D. Stone, J.D. Joannopoulos, M. Soljačić, Bound states in the continuum, Nat. Rev. Mater. 1 (2016) 16048. https://doi.org/10.1038/natrevmats.2016.48.
[24] A.A. Lyapina, D.N. Maksimov, A.S. Pilipchuk, A.F. Sadreev, Bound states in the continuum in open acoustic resonators, J. Fluid. Mech. 780 (2015) 370–387. https://doi.org/10.1017/jfm.2015.480.
[25] E.H. El Boudouti, T. Mrabti, H. Al-Wahsh, B. Djafari-Rouhani, A. Akjouj, L. Dobrzynski, Transmission gaps and Fano resonances in an acoustic waveguide: analytical model, J. Phys.: Conden. Mat. 20 (2008) 255212. https://doi.org/10.1088/0953-8984/20/25/255212.
[26] H.Q. Nguyen, Q. Wu, H. Chen, J.J. Chen, Y.K. Yu, S. Tracy, G.L. Huang, A Fano-based acoustic metamaterial for ultra-broadband sound barriers, Proceedings of the Royal Society A: Mathematical, Phys. Eng. Sci. 477 (2021) rspa.2021.0024. https://doi.org/10.1098/rspa.2021.0024.
[27] L. Xiong, W. Bi, Y. Aurégan, Fano resonance scatterings in waveguides with impedance boundary conditions, J. Acoust. Soc. Am. 139 (2016) 764–772. https://doi.org/10.1121/1.4941568.
[28] M. Amin, O. Siddiqui, M. Farhat, A. Khelif, A perfect Fresnel acoustic reflector implemented by a Fano-resonant metascreen, J. Appl. Phys. 123 (2018) 144502. https://doi.org/10.1063/1.5012012.
[29] A. Merkel, G. Theocharis, O. Richoux, V. Romero-García, V. Pagneux, Control of acoustic absorption in one-dimensional scattering by resonant scatterers, Appl. Phys. Lett. 107 (2015) 244102. https://doi.org/10.1063/1.4938121.
[30] L. Chesnel, S.A. Nazarov, Non reflection and perfect reflection via Fano resonance in waveguides, Commun. Math. Sci. 16 (2018) 1779–1800. https://doi.org/10.4310/CMS.2018.V16.N7.A2.
[31] T. Lee, T. Nomura, X. Su, H. Iizuka, Fano-Like Acoustic Resonance for Subwavelength Directional Sensing: 0–360 Degree Measurement, Adv. Sci. 7 (2020) 1–9. https://doi.org/10.1002/advs.201903101.
[32] Y.Y. Sun, J.P. Xia, H.X. Sun, S.Q. Yuan, Y. Ge, X.J. Liu, Dual-Band Fano Resonance of Low-Frequency Sound Based on Artificial Mie Resonances, Advanced Science. 6 (2019). https://doi.org/10.1002/advs.201901307.
[33] E. Kamenetskii, A.E. Sadreev, A. Miroshnichenko, Fano Resonances in Optics and

Microwaves, Springer International Publishing, Cham, 2018. https://doi.org/10.1007/978-3-319-99731-5.

[34] Z.X. Xu, B. Zheng, J. Yang, B. Liang, J.C. Cheng, Machine-Learning-Assisted Acoustic Consecutive Fano Resonances: Application to a Tunable Broadband Low-Frequency Metasilencer, Phys. Rev. Appl. 16 (2021) 1. https://doi.org/10.1103/PhysRevApplied.16.044020.

[35] A. Biçer, M. Günay, N. Korozlu, A. Cicek, Continuously tunable acoustic Fano resonance in side-coupled Helmholtz resonator array assisted by a surface phononic crystal, Appl. Phys. Lett. 120 (2022). https://doi.org/10.1063/5.0072281.

[36] Y. Jin, E.H. EI Boudouti, Y. Pennec, B. Djafari-Rouhani, Tunable Fano resonances of Lamb modes in a pillared metasurface, J. Phys. D. Appl. Phys. 50 (2017) 425304. https://doi.org/10.1088/1361-6463/aa8a19.

[37] S. Hayashi, D. V. Nesterenko, A. Rahmouni, Z. Sekkat, Polarization effects in light-tunable Fano resonance in metal-dielectric multilayer structures, Phys. Rev. B. 95 (2017) 1–8. https://doi.org/10.1103/PhysRevB.95.165402.

[38] X. Wang, G. Liu, S. Xia, H. Meng, X. Shang, P. He, X. Zhai, Dynamically Tunable Fano Resonance Based on Graphene Metamaterials, IEEE Photon. Tech. Let. 30 (2018) 2147–2150. https://doi.org/10.1109/LPT.2018.2879540.

[39] B. Liu, C. Tang, J. Chen, M. Zhu, M. Pei, X. Zhu, Electrically Tunable Fano Resonance from the Coupling between Interband Transition in Monolayer Graphene and Magnetic Dipole in Metamaterials, Sci. Rep. (2017) 1–8. https://doi.org/10.1038/s41598-017-17394-y.

[40] A. Bhardwaj, V. Sridurai, N.M. Puthoor, A.B. Nair, T. Ahuja, G.G. Nair, Evidence of Tunable Fano Resonance in a Liquid Crystal-Based Colloidal Metamaterial, Adv. Opt. Mater. 8 (2020) 1–9. https://doi.org/10.1002/adom.201901842.

[41] W. Zhao, H. Jiang, B. Liu, Y. Jiang, C. Tang, J. Li, Fano resonance based optical modulator reaching 85% modulation depth, Appl. Phys. Lett. 107 (2015). https://doi.org/10.1063/1.4935031.

[42] M. Zilletti, P. Gardonio, Experimental implementation of switching and sweeping tuneable vibration absorbers for broadband vibration control, J. Sound. Vib. 334 (2015) 164–177. https://doi.org/10.1016/j.jsv.2014.09.005.

[43] S. Miani, M. Zilletti, P. Gardonio, F. Blanchini, P. Colaneri, Switching and sweeping vibration absorbers: Theory and experimental validation, Automatica. 93 (2018) 290–301. https://doi.org/10.1016/j.automatica.2018.03.021.

[44] Y. Zhang, Towards altering sound frequency at will by a linear meta-layer with time-varying and quantized properties, Commun. Phys. (n.d.) 311300. https://doi.org/10.1038/s42005-021-00721-1.

[45] L. Huang, K. Wu, X. Han, Y. Zhang, Mechanism of low frequency spectral scattering by a side-branch electromagnetic device with switching shunt, J. Sound. Vib. 545 (2023) 117423. https://doi.org/10.1016/j.jsv.2022.117423.

[46] L. Dal Bo, P. Gardonio, D.E. Casagrande, S. Saggini, Smart panel with sweeping and switching piezoelectric patch vibration absorbers: Experimental results, Mech. Syst. Signal Process. 120 (2019) 308–325. https://doi.org/10.1016/j.ymssp.2018.10.024.

[47] P. Gardonio, G. Konda Rodrigues, L. Dal Bo, E. Turco, Extremum seeking online tuning

of a piezoelectric vibration absorber based on the maximisation of the shunt electric power absorption, Mech. Syst. Signal. Process. 176 (2022) 109171. https://doi.org/10.1016/j.ymssp.2022.109171.

[48] M.B. Zanjani, A.R. Davoyan, A.M. Mahmoud, N. Engheta, J.R. Lukes, One-way phonon isolation in acoustic waveguides, Appl. Phys. Lett. 104 (2014). https://doi.org/10.1063/1.4866590.

[49] R.L. Thomes, D. Beli, C.D.M. Junior, Space – time wave localization in electromechanical metamaterial beams with programmable defects, Mech. Syst. Signal Process. 167 (2022) 108550. https://doi.org/10.1016/j.ymssp.2021.108550.

[50] R. Sarban, R.W. Jones, B.R. MacE, E. Rustighi, A tubular dielectric elastomer actuator: Fabrication, characterization and active vibration isolation, Mech. Syst. Signal Process. 25 (2011) 2879–2891. https://doi.org/10.1016/j.ymssp.2011.06.004.

[51] Z. Chen, S. Sun, L. Deng, J. Yang, S. Zhang, H. Du, W. Li, Investigation of a new metamaterial magnetorheological elastomer isolator with tunable vibration bandgaps, Mech. Syst. Signal Process. 170 (2022) 108806. https://doi.org/10.1016/j.ymssp.2022.108806.

[52] J.A.B. Gripp, D.A. Rade, Vibration and noise control using shunted piezoelectric transducers: A review, Mech. Syst. Signal Process. 112 (2018) 359–383. https://doi.org/10.1016/j.ymssp.2018.04.041.

[53] K. Wu, L. Huang, X. Zhang, X. Liu, C. Wang, Y. Zhang, Broadband and extremely low frequency sound isolation by a programmable shunted electromechanical diaphragm with force dipole effect, Int. J. Mech. Sci. 200 (2021) 106447. https://doi.org/10.1016/j.ijmecsci.2021.106447.

[54] Y. Zhang, C. Wang, L. Huang, A tunable electromagnetic acoustic switch, Appl. Phys. Lett. 116 (2020) 183502. https://doi.org/10.1063/5.0008532.

[55] Y. Zhang, C. Wang, L. Huang, Tuning of the acoustic impedance of a shunted electro-mechanical diaphragm for a broadband sound absorber, Mech. Syst. Signal Process. 126 (2019) 536–552. https://doi.org/10.1016/j.ymssp.2019.02.049.

[56] E. Turco, P. Gardonio, L.D. Bo, Tuning of a shunted electromagnetic vibration absorber based on the maximisation of the electrical power dissipated, Proc. .Inst. Mech. Eng., Part C: J. Mech. Engin. Sci. 235 (2021), 2570-2586. https://doi.org/10.1177/0954406221991182.

[57] E. Turco, P. Gardonio, R. Petrella, L. Dal Bo, Modular Vibration Control Unit Formed by an Electromagnetic Proof-Mass Transducer and Sweeping Resistive–Inductive Shunt, J. Vib. Acoust. 142 (2020). https://doi.org/10.1115/1.4047068.

[58] Y. Zhang, L. Huang, Realization of Resonance of a Diaphragm at Any Desired Frequency, J. Mech. 34 (2018) 29–34. https://doi.org/10.1017/jmech.2015.105.

[59] Y. Zhu, D.J. Gauthier, S.E. Morin, Q. Wu, H.J. Carmichael, T.W. Mossberg, Vacuum Rabi splitting as a feature of linear-dispersion theory: Analysis and experimental observations, Phys. Rev. Lett. 64 (1990) 2499–2502. https://doi.org/10.1103/PhysRevLett.64.2499.

[60] G. Khitrova, H.M. Gibbs, M. Kira, S.W. Koch, A. Scherer, Vacuum Rabi splitting in semiconductors, Nat. Phys. 2 (2006) 81–90. https://doi.org/10.1038/nphys227.

[61] J.Y. Chung, D.A. Blaser, Transfer function method of measuring in-duct acoustic properties. I. Theory, J. Acoust. Soc. Am. 68 (1980) 907–913.

https://doi.org/10.1121/1.384778.
[62] J.Y. Chung, D.A. Blaser, Transfer function method of measuring in-duct acoustic properties. II. Experiment, J. Acoust. Soc. Am. 68 (1980) 914–921. https://doi.org/10.1121/1.384779.